Global Biogeochemical Cycles

RESEARCH ARTICLE
10.1029/2020GB006562

Key Points:
- Dust fluxes to the South Pacific Gyre are quantified using measurements of dissolved and particulate thorium isotopes
- Global models underestimate dust flux to the South Pacific Gyre by 1–2 orders of magnitude
- Dust deposition is the most important source of dissolved iron to the surface of the South Pacific Ocean

Correspondence to:
F. J. Pavia,
fjpavia@caltech.edu

Citation:
Pavia, F. J., Anderson, R. F., Winckler, G., & Fleisher, M. Q. (2020). Atmospheric dust inputs, iron cycling, and biogeochemical connections in the South Pacific Ocean from thorium isotopes. *Global Biogeochemical Cycles*, *34*, e2020GB006562. https://doi.org/10.1029/2020GB006562

Received 24 JAN 2020
Accepted 3 AUG 2020
Accepted article online 6 AUG 2020

Atmospheric Dust Inputs, Iron Cycling, and Biogeochemical Connections in the South Pacific Ocean From Thorium Isotopes

Frank J. Pavia[1,2,3], Robert F. Anderson[1,2], Gisela Winckler[1,2], and Martin Q. Fleisher[1]

[1]Lamont-Doherty Earth Observatory of Columbia University, Palisades, NY, USA, [2]Department of Earth and Environmental Sciences, Columbia University, New York, NY, USA, [3]Now at Division of Geological and Planetary Sciences, California Institute of Technology, Pasadena, CA, USA

Abstract One of the primary sources of micronutrients to the sea surface in remote ocean regions is the deposition of atmospheric dust. Geographic patterns in biogeochemical processes such as primary production and nitrogen fixation that require micronutrients like iron (Fe) are modulated in part by the spatial distribution of dust supply. Global models of dust deposition rates are poorly calibrated in the open ocean, owing to the difficulty of determining dust fluxes in sparsely sampled regions. We present new estimates of dust and Fe input rates from measurements of dissolved and particulate thorium isotopes ^{230}Th and ^{232}Th on the *FS Sonne* SO245 section (GEOTRACES process study GPpr09) in the South Pacific. We first discuss high-resolution upper water column profiles of Th isotopes and the implications for the systematics of dust flux reconstructions from seawater Th measurements. We find dust fluxes in the center of the highly oligotrophic South Pacific Gyre that are the lowest of any mean annual dust input rates measured in the global oceans, but that are 1–2 orders of magnitude higher than those estimated by global dust models. We also determine dust-borne Fe fluxes and reassess the importance of individual Fe sources to the surface South Pacific Gyre, finding that dust dissolution, not vertical or lateral diffusion, is the primary Fe source. Finally, we combine our estimates of Fe flux in dust with previously published cellular and enzymatic quotas to determine theoretical upper limits on annual average nitrogen fixation rates for a given Fe deposition rate.

1. Introduction

Wind-blown mineral dust deposition provides a unique source of micronutrients to remote ocean regions, acting as a regulator of global biogeochemistry and elemental cycling in both the modern ocean (Jickells et al., 2005) and in the geologic past (Lamy et al., 2014; Martínez-Garcia et al., 2014). Much of the biogeochemical significance of dust hinges on it being a source of iron (Fe), an element that limits primary productivity in ~30% of the global ocean (Moore et al., 2013). Many other biochemical processes conducted by marine phytoplankton also utilize Fe, most notably nitrogen fixation (Moore et al., 2009) using nitrogenase, an enzyme with one of the highest Fe requirements found in nature (Whittaker et al., 2011).

The South Pacific Ocean is a particularly important region for understanding dust and Fe inputs. The South Pacific Gyre (SPG) is among the most oligotrophic oceanic regions, with pervasive nutrient limitation of productivity (Bonnet et al., 2008), the lowest satellite-derived chlorophyll a estimates (e.g. Claustre et al., 2008), and lowest modeled dust inputs (Mahowald et al., 2005) in the ocean. Inverse models have predicted significant N_2-fixation rates for the SPG given the vanishingly low surface nitrate concentrations and proximity to coastal oxygen minimum zones of intense fixed N loss (Deutsch et al., 2007). However, incubation studies typically find much lower N_2-fixation rates in the SPG, a discrepancy that has been attributed to Fe-limitation of diazotrophs (Knapp et al., 2016).

A comprehensive understanding of the feedbacks between dust fluxes, iron input, and biogeochemical processes like N_2-fixation in the South Pacific is still lacking. This is in part because global models of dust input and iron dynamics still have significant uncertainties. Dust deposition models have few observational constraints over the open ocean, particularly in the South Pacific, given its remoteness from the continents and

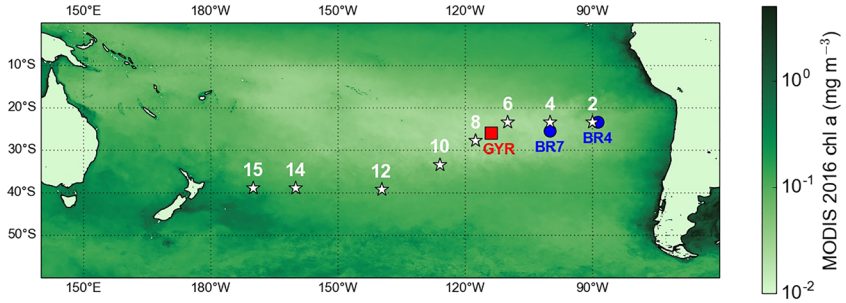

Figure 1. Sitemap of SO245 sampling locations (white stars), as well as locations of dissolved Fe data (Fitzsimmons et al., 2016) from BiG RAPA (BR, stations 4 and 7, blue dots) and from BIOSOPE GYR station (Blain et al., 2008) with 2016 annually averaged satellite-derived chlorophyll a derived from the Moderate Resolution Imaging Spectroradiometer (MODIS) (data doi: 10.5067/AQUA/MODIS/L3B/CHL/2018).

lack of well-dated surface sediments (Albani et al., 2014; Costa et al., 2020; Kienast et al., 2016). Different global iron models vary over orders of magnitude in their simulated deposition rates from dust and in their average water column residence times of dissolved iron (Tagliabue et al., 2016). Observations of modern dust deposition and iron input rates, as well as iron residence times, would be of great use in constraining these models, thus improving their ability to simulate biogeochemical feedbacks between iron input and the activity of marine phytoplankton.

Long-lived thorium isotopes in the ocean are highly sensitive tracers of particle flux and have recently been deployed as tracers of modern dust inputs (Anderson et al., 2016; Deng et al., 2014; Hayes et al., 2017; Hayes, Anderson, Fleisher, et al., 2013; Hsieh et al., 2011; Lopez et al., 2015) and further exploited to constrain residence times of dissolved trace metals, including Fe (Hayes et al., 2015; Hayes, Anderson, et al., 2018). While one long-lived Th isotope (^{230}Th) is produced in the water column at a constant and precisely known rate by ^{234}U decay, the other (^{232}Th) is primordial and brought to the ocean via the dissolution of lithogenic materials. Thorium is extremely particle reactive and is rapidly removed from solution by adsorption onto sinking particulate matter (Moore & Sackett, 1964). Since it is removed so quickly, it is typically assumed that dissolved ^{230}Th is negligibly redistributed by physical processes, so a 1-D mass budget can be easily constructed between its production by ^{234}U decay and its removal onto sinking particles (Bacon & Anderson, 1982). Applying this 1-D mass budget derived from radiogenic ^{230}Th to the primordial isotope ^{232}Th, which shares identical scavenging behavior to ^{230}Th, allows for the determination of ^{232}Th (and thus, dust) input rates (Hayes, Anderson, Fleisher, et al., 2013; Hirose & Sugimura, 1987; Hsieh et al., 2011).

In this study, we present new high-resolution measurements of dissolved ^{230}Th and ^{232}Th from the upper water column, as well as particulate ^{230}Th and ^{232}Th measurements, from the South Pacific Ocean between Chile and New Zealand. We first discuss the implications of the dissolved and particulate Th distributions for two different methodologies for determining dust fluxes from water column Th observations. We then use our observations to compute dust input rates, iron fluxes, and iron residence times in the South Pacific and derive an upper bound of N_2-fixation rates that can be supported for a given Fe supply, with implications for diazotrophy in the SPG.

2. Materials and Methods

2.1. Cruise Track and Sample Collection

Samples were collected aboard the *FS Sonne* cruise SO245 on the UltraPac transect between Antofagasta, Chile and Wellington, New Zealand from December 2015 to January 2016 (Figure 1). Ten-liter samples for dissolved ^{230}Th and ^{232}Th were collected from Niskin bottles deployed on a stainless steel rosette, filtered through 0.45 μm Acropak capsule filters into acid-cleaned 10 L cubitainers, and immediately acidified to pH ~ 1.8 using 40 ml of 6 M hydrochloric acid.

Particulate samples were collected via in situ filtration using McLane pumps (WTS-LV). Each sample was pumped through a 142-mm-diameter filter holder with a titanium baffle used to generate homogenous particle distributions. Samples were collected on paired acid-leached 0.8 μm Pall Supor 800 polyethersulfone

filters. Blank filters were deployed along with the pumps on each cast, in a cut-open Ziploc plastic bag zip-tied to the frame of a pump to allow blank filters to be in contact with ambient seawater for the duration of the pump deployment.

2.2. Sample Analysis

A 5 L aliquot of each 10 L dissolved sample was transferred to a new acid-cleaned cubitainer. A ^{229}Th spike and 15 mg of dissolved Fe carrier were added to each sample. The spikes were allowed to equilibrate for 24 hr before sample pH was raised to ~8.5 to precipitate Fe. The resulting Fe precipitate was concentrated, washed in Milli-Q water, and digested at 200°C using concentrated HNO_3, HF, and $HClO_4$. Thorium isotopes were then isolated via anion exchange chromatography on Bio-rad AG1-X8 100-200 mesh size resin. Concentrations of ^{230}Th and ^{232}Th were measured by isotope dilution using a Thermo ELEMENT XR ICP-MS in peak jumping mode (Anderson et al., 2012).

Procedural blanks for dissolved Th isotopes were determined by processing 3–5 L of Milli-Q water in acid-cleaned cubitainers under identical methods. Half the blanks were taken to sea and acidified to pH = 2 along with seawater samples, and half the blanks were acidified in the lab. No statistically significant difference was observed between sea blanks and lab blanks processed in this manner. The average of all ($n = 22$) procedural blanks run during the measurement of SO245 samples was used to correct the sampleconcentrations. Mean and 1σ blanks for dissolved Th isotopes were ^{232}Th = 7.4 ± 5.4 pg and ^{230}Th = 0.47 ± 0.39 fg. Reproducibility was determined by measuring aliquots of two intercalibrated standard solutions of Th isotopes, SW STD 2010-1 (Anderson et al., 2012) and SW STD 2015-1. For standards run alongside SO245 samples, the reproducibility for each isotope was 0.71% for ^{230}Th and 1.09% for ^{232}Th on SW STD 2010-1 and was 0.47% for ^{230}Th and 2.26% for ^{232}Th on SW STD 2015-1.

Particulate Th isotopes were analyzed similarly to previously described methods (Pavia et al., 2018, 2019). The top 0.8 μm Supor filter from each sample was folded into a 60 ml Teflon jar, where ^{229}Th spike and 7–8 mg of dissolved Fe carrier were added. The filters sat overnight at room temperature in 5 ml concentrated HNO_3, before complete digestion at 220°C using concentrated $HClO_4$ and HF. After complete dissolution, samples underwent an Fe coprecipitation, the precipitate of which was subsequently washed, redissolved, and taken through anion exchange chromatography to isolate Th isotopes. Measurement of particulate ^{230}Th and ^{232}Th concentrations was performed by isotope dilution under similar conditions as dissolved Th concentrations. The pooled average concentration of ^{232}Th and ^{230}Th in all analyzed dipped blank filters (^{232}Th = 8.7 ± 4.3 pg and ^{230}Th = 1.6 ± 0.7 fg; $n = 8$) was used to correct measured particulate Th concentrations.

Corrections were made to both dissolved and particulate data to isolate the ^{230}Th produced by ^{234}U decay in the water column ($^{230}Th_{xs}$). This includes previously described (Hayes, Anderson, Jaccard, et al., 2013; Pavia et al., 2018) corrections to dissolved ^{230}Th for ingrowth during sample storage and for lithogenic contributions. While the corrected $^{230}Th_{xs}$ data are used for all calculations described in this paper, the subscript *xs* is henceforth omitted for clarity.

3. Background: Calculating Dust Fluxes

Two methods have been proposed for determining dust fluxes from water column measurements of thorium isotopes (Anderson et al., 2016). The two methods share some assumptions, namely, that the one-dimensional budget for ^{230}Th is a simple mass balance between ^{234}U decay and scavenging removal onto particles. However, there are also several assumptions unique to each method. Here, we outline the measurements, calculations, and primary uncertainties involved in determining dust fluxes using thorium isotopes.

3.1. Dust Fluxes From Dissolved ^{230}Th-^{232}Th

When dust is deposited at the surface ocean, elements in the lithogenic matrix partially dissolve into solution. For nonbioactive elements with a sufficiently short scavenging residence time to prevent net lateral redistribution, it can be assumed that the upper water column mass budget for these elements reflects a balance between dust dissolution and scavenging removal. By measuring mixed layer concentrations of

aluminum (Al), and assuming both a fractional solubility and a scavenging removal rate, early work attempted to exploit this mass budget to calculate dust input rates (Measures & Brown, 1996; Measures & Vink, 2000).

Like Al, ^{232}Th is predominantly supplied to the surface ocean of regions far from continental shelves by dust deposition. Unlike Al, there is also a radiogenic isotope of thorium, ^{230}Th, produced in the water column at a known rate by ^{234}U decay. Neglecting lateral redistribution, the residence time of Th (τ_z) integrated to depth z can be computed by dividing the water column inventory of ^{230}Th by its vertically integrated production rate (note that inventory and production rate are in activity units):

$$\tau_z = \frac{\int_0^z {}^{230}\mathrm{Th}_d \, dz}{\int_0^z {}^{234}\mathrm{U}^*\lambda_{230} \, dz}. \quad (1)$$

Assuming that ^{230}Th and ^{232}Th have identical chemical scavenging behavior (e.g., physical speciation and reactivity), the thorium residence time derived from ^{230}Th can then be applied to ^{232}Th (Hayes, Anderson, Fleisher, et al., 2013; Hirose & Sugimura, 1987; Hsieh et al., 2011). The determination of this residence time circumvents the problems associated with assuming a scavenging residence time for dust flux estimates using Al. Dividing the inventory of dissolved ^{232}Th by the residence time derived from ^{230}Th allows for computation of the ^{232}Th flux:

$$F\left({}^{232}\mathrm{Th}\right) = \frac{\int_0^z {}^{232}\mathrm{Th}_d \, dz}{\tau_z}. \quad (2)$$

By assuming that the 1-D mass budget of dissolved ^{232}Th reflects a balance between dust dissolution and scavenging removal, the ^{232}Th flux can be converted into a dust flux through dividing by a fractional Th solubility (S_{Th}) and the concentration of ^{232}Th in the dust ($[^{232}\mathrm{Th}]_{\mathrm{dust}}$):

$$\text{Dust Flux} = \frac{F\left({}^{232}\mathrm{Th}\right)}{S_{\mathrm{Th}} * \left[{}^{232}\mathrm{Th}\right]_{\mathrm{dust}}}. \quad (3)$$

3.2. Dust Fluxes From Particulate ^{230}Th-^{232}Th

A second approach to calculate dust fluxes involves measuring ^{230}Th and ^{232}Th on particulate matter in the water column. This method also relies on the assumption that the integrated production of ^{230}Th to depth z by uranium decay is balanced by its removal on particulate matter sinking through that depth. Thus, the ^{230}Th on particulate material is an integration of all the dissolved ^{230}Th produced in the overlying water column. The apparent dust flux at depth z can be calculated by dividing the integrated ^{230}Th production rate by the particulate ^{230}Th concentration at z, multiplying by the particulate ^{232}Th concentration at z, and dividing by the ^{232}Th concentration in dust:

$$\text{Dust Flux} = \frac{\int_0^z {}^{234}\mathrm{U} * \lambda_{230} \, dz}{\left[{}^{230}\mathrm{Th}\right]_p^z} * \frac{\left[{}^{232}\mathrm{Th}\right]_p^z}{\left[{}^{232}\mathrm{Th}\right]_{\mathrm{dust}}}. \quad (4)$$

4. Results

4.1. Dissolved and Particulate ^{230}Th

Dissolved ^{230}Th ($^{230}\mathrm{Th}_d$) profiles have constant values of 0.2–0.8 μBq/kg in the upper 100–200 m, before linearly increasing with depth toward values of 2.5–5 μBq/kg at 500 m (Figure 2a). The depths at which upper water column $^{230}\mathrm{Th}_d$ remains constant in the uppermost water column vary among stations. For stations 2 through 10, depth at which ^{230}Th begins to increase generally follows the depth of the deep chlorophyll maximum (DCM) at each station, at depths of ~180–200 m at stations 4–8 and ~120 m at stations 2 and 10. This is consistent with high-resolution $^{230}\mathrm{Th}_d$ profiles from the upper water column at Station Aloha in the subtropical North Pacific (Hayes et al., 2015) and subtropical North Atlantic (Hayes et al., 2017). This relationship

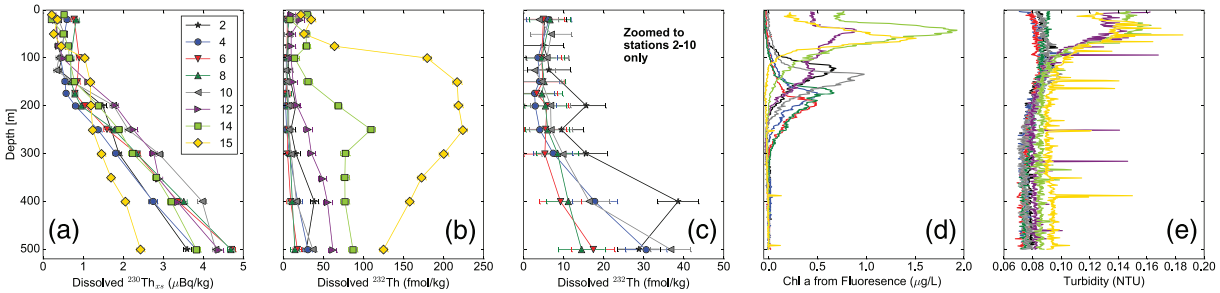

Figure 2. Upper water column profiles from SO245. (a) Dissolved ^{230}Th, (b) dissolved ^{232}Th, (c) same as (b) but only stations 2–10 with zoomed *x*-axis, (d) chlorophyll concentrations from fluorescence data (WET Labs ECO-FL Fluorometer) binned at 1 m intervals, and (e) turbidity (WET Labs ECO-FL-NTU Turbidity Meter). Chlorophyll fluorescence and turbidity data can be found on Pangaea (https://doi.pangaea.de/10.1594/PANGAEA.890394).

is somewhat more complicated at stations 12–15, furthest west on the SO245 transect. These stations had significantly higher chlorophyll fluorescence at the surface, and high turbidity between the surface and 100 m, indicating greater particle abundance and productivity (Figures 2c and 2d). At station 12, $^{230}Th_d$ increases starting at 100 m, aligning with the base of the surface-most fluorescence peak, and at stations 14 and 15, $^{230}Th_d$ begins increasing at the depth where fluorescence returns to background levels. This pattern was also observed at station 2 of Hayes et al. (2017), which similarly had high surface fluorescence above the DCM.

Between the DCM and 1,500 m, $^{230}Th_d$ generally increases linearly with depth (Figure 3a), as expected from reversible scavenging (Bacon & Anderson, 1982). The slope of this increase with depth varies from station to station, reflecting the integrated scavenging intensity. Stations 12, 14, and 15, with the highest chlorophyll fluorescence and turbidity at the sea surface, reflecting the greatest particle flux, have the lowest $^{230}Th_d$ values at 1,500 m of 7–10 μBq/kg (Figure 3a). There is also a gradient between the stations nearest to the South American coast, with $^{230}Th_d$ at 1,500 m increasing from 13 μBq/kg at station 2 to 16–17 μBq/kg at stations 4, 6, and 8. Like $^{230}Th_d$, particulate ^{230}Th ($^{230}Th_p$) tends to increase linearly with depth between the DCM and 2,000 m, with values < 0.5 μBq/kg at and above the DCM, and values of 1.6–3.4 μBq/kg at 2,000 m (Figure 3c).

4.2. Dissolved and Particulate ^{232}Th

Dissolved ^{232}Th ($^{232}Th_d$) at stations 4–10 show consistent profile shapes with constant, low ^{232}Th of 2–10 fmol/kg in the upper 300 m increasing to 15–35 fmol/kg at 500 m (Figures 2b and 2c). These surface $^{232}Th_d$ concentrations are four to 10 times lower than at the surface of Station Aloha in the subtropical North Pacific (Hayes et al., 2015). At station 2, $^{232}Th_d$ is also ~5 fmol/kg in the upper 120 m, then steadily increases toward 30 fmol/kg between 120 and 500 m (Figures 2b and 2c). Like for $^{230}Th_d$, stations 12–15 have much different ^{232}Th profiles (Figure 2b). Except for a single high $^{232}Th_d$ value of 20 fmol/kg at 20 m, $^{232}Th_d$ at station 12 is constant at 10 fmol/kg from 0 to 150 m, then increases linearly below 150 m to 60 fmol/kg at 500 m. Station 14 has variable $^{232}Th_d$ between 10 and 30 fmol/kg in the upper 150 m, then increases toward a

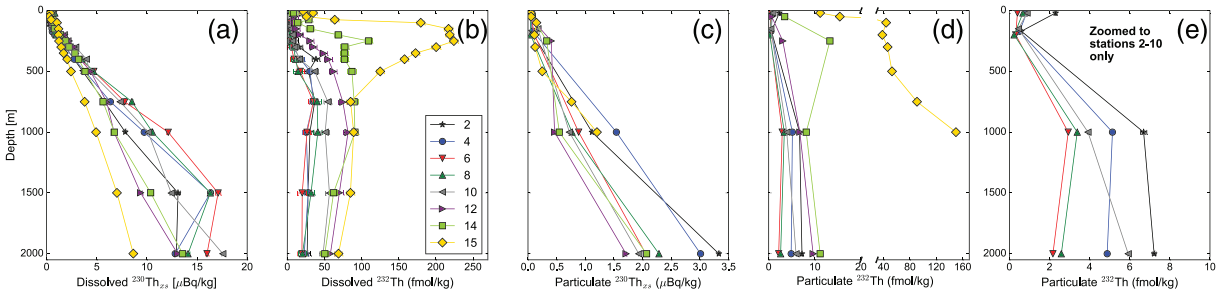

Figure 3. Upper 2,000 m depth profiles from SO245. (a) Dissolved ^{230}Th, (b) dissolved ^{232}Th, (c) particulate ^{230}Th, (d) particulate ^{232}Th, and (e) same as (d) but only stations 2–10 with zoomed *x*-axis.

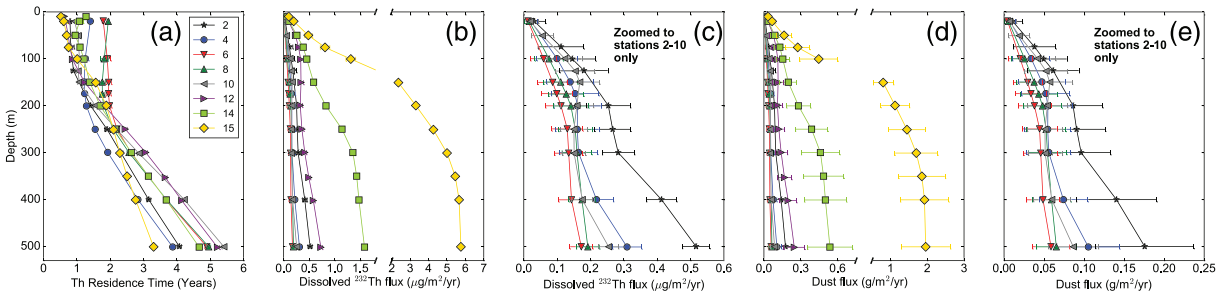

Figure 4. Upper water column profiles of parameters derived from paired dissolved Th isotopes. (a) Thorium residence time calculated using Equation 1, (b) dissolved ^{232}Th flux calculated Equation 2, (c) same as (b) but only stations 2–10 with zoomed *x*-axis. (d) Dust flux calculated using Equation 3, with 14 ± 1 ppm for $[^{232}\text{Th}]_{\text{dust}}$ and $S_{\text{Th}} = 0.21 \pm 0.07$, and (e) same as (d) but only stations 2–10 with zoomed *x*-axis.

maximum of 110 fmol/kg at 250 m, before reaching constant values of 80–90 fmol/kg from 250 to 500 m. Station 15 has similarly high $^{232}\text{Th}_d$ of 25 fmol/kg in the upper 50 m, then increases sharply toward a broad maximum of 220 fmol/kg between 150 and 250 m, before decreasing to 130 fmol/kg at 500 m.

Below 500 m, $^{232}\text{Th}_d$ at stations 2–8 continues to increase with depth, reaching peak values of 35 fmol/kg at 750 m before decreasing to 20 fmol/kg at 1,500 m (Figure 3b). At stations 10 and 12, the $^{232}\text{Th}_d$ values at 750 m are higher, at 55 and 75 fmol/kg, respectively, and remain roughly constant to 1,500 m. The $^{232}\text{Th}_d$ at station 14 increases from 80 fmol/kg at 300 m to 90 fmol/kg at 750–1,000 m, before decreasing to 60 fmol/kg at 1,500 m. At station 15, $^{232}\text{Th}_d$ decreases from its maximum value of 220 fmol/kg at 250 m to a constant value of 90 fmol/kg between 750 and 1,500 m.

Particulate ^{232}Th ($^{232}\text{Th}_p$) decreases slightly from the surface to the DCM at all of stations 2–10, with values of 0.4–2.3 fmol/kg at 20 m and 0.24–0.6 fmol/kg at the DCM (Figures 3d and 3e). The $^{232}\text{Th}_p$ at each of these stations then increases to constant values of 2–7 fmol/kg at 1,000–2,000 m. Highest $^{232}\text{Th}_p$ between stations 2 and 10 is found at stations 2 and 10, followed by station 4, with the lowest concentrations found at stations 6 and 8. At station 12, $^{232}\text{Th}_p$ increases from 0.67 fmol/kg at the surface to 9.6 fmol/kg at 2,000 m, while at station 14, there is a subsurface $^{232}\text{Th}_p$ maximum of 13.3 fmol/kg at 250 m (Figure 3d). Station 15 was the only location where a high-resolution profile of particulate Th isotopes was collected. Here, the highest surface $^{232}\text{Th}_p$ concentrations of the entire transect were observed at 11 fmol/kg. Concentrations increased to 43.8 fmol/kg at 100 m, increasing further to 52.8 fmol/kg at 500 m, then increasing steeply to 150 fmol/kg between 500 and 1,000 m.

5. Discussion

5.1. Upper Water Column Th Dynamics

5.1.1. Depth Dependence of ^{232}Th and Dust Fluxes

Depth-integrated residence times for thorium (τ) are computed using Equation 1. The depth profile of τ follows the same pattern at each station (Figure 4a) as the depth pattern of $^{230}\text{Th}_d$ (Figure 2a). Near-surface τ is 0.5–2 years, is constant with depth in the upper 100–200 m, then increases linearly with depth down to 500 m (Figure 4a). There are also vertical trends in profiles of depth-integrated dissolved ^{232}Th flux computed using Equation 2 (Figure 4b). If both dissolved Th isotopes were scavenged with uniform and consistent rate constants throughout the water column, and if $^{232}\text{Th}_d$ were only supplied at the sea surface by dust dissolution, then vertical profiles of dissolved ^{232}Th flux would be constant with depth, as required by mass balance. In section 5.1.2, we argue that increasing ^{232}Th fluxes with depth are an artifact associated with vertical mixing of dissolved ^{230}Th in the mixed layer, but we first describe the other hypotheses that have been put forward to explain this feature.

The depth dependence of ^{232}Th flux profiles introduces complications for comparing dissolved thorium-derived dust fluxes with estimates from other methods and models, as an integration depth must be chosen as representative of the true dust flux. Which integration depth is right? Previous studies have deployed a variety of different integration strategies. Hsieh et al. (2011) only integrated within the mixed layer to avoid possible complications from lateral advection of nonlocal ^{232}Th in the shallow subsurface.

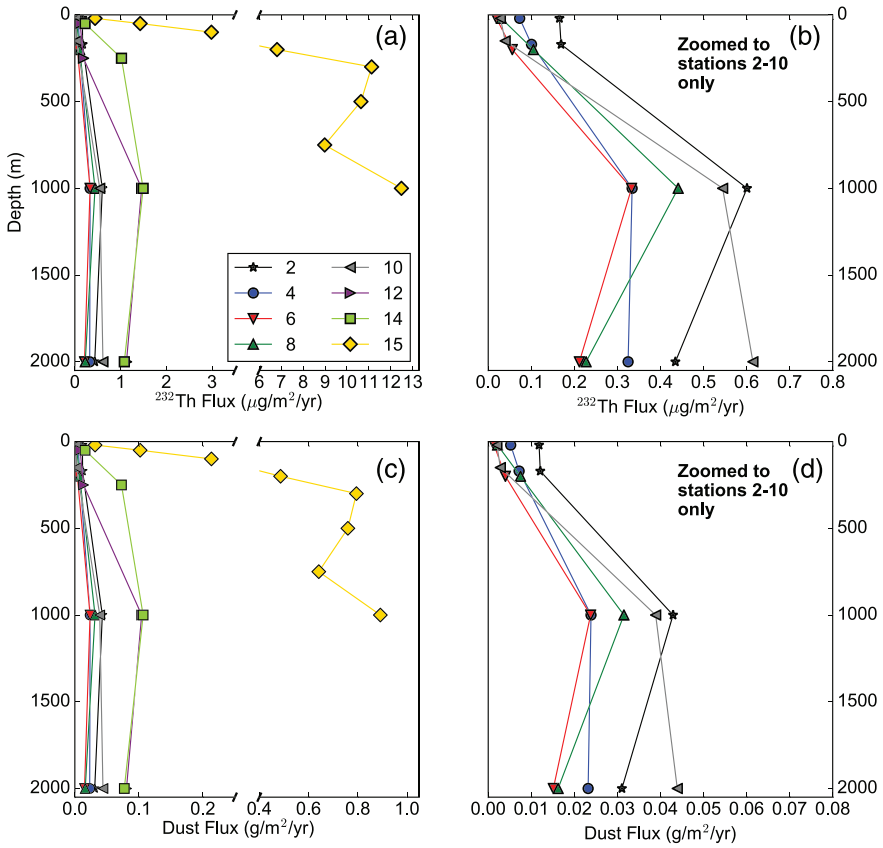

Figure 5. Profiles of parameters derived from paired particulate Th isotopes. (a) ^{232}Th flux, (b) same as (a) but with *x*-axis zoomed to more clearly see vertical patterns at stations 2–10. (c) Dust flux calculated using Equation 4, with 14 ± 1 ppm for $[^{232}\text{Th}]_{\text{dust}}$. (d) Same as (c) but with *x*-axis zoomed to more clearly see vertical patterns at stations 2–10.

Hayes, Anderson, Fleisher, et al. (2013) and Lopez et al. (2015) chose 500 m to average any seasonal variability in ^{232}Th deposition and reduce possible uncertainties associated with vertical transport of ^{230}Th into the mixed layer. More recent studies have argued for an intermediate approach of using 250 m (Deng et al., 2014) or the base of the euphotic zone/DCM (Hayes et al., 2017).

The choice of integration depth would ideally not be subjective, but based on objective criteria derived from an understanding of the mechanisms that drive increasing ^{232}Th fluxes with depth. Several mechanisms have been put forward to explain increasing apparent dissolved ^{232}Th fluxes with depth. One, that ^{232}Th is preferentially bound in rapidly cycled colloids compared to ^{230}Th, has largely been ruled out on the basis of similar fractions of colloidal ^{230}Th and ^{232}Th between the surface and 1,000 m, albeit with limited data to date (Hayes et al., 2015, 2017).

More recently, Hayes et al. (2017) suggested that rapid, nonreversible ^{230}Th removal coincident with particulate organic carbon export from the euphotic zone could explain the constant τ and increasing ^{232}Th flux from the surface to the DCM in the subtropical North Atlantic. This suggestion was made on the basis of constant dissolved ^{230}Th concentrations found between the sea surface and DCM. However, this mechanism cannot explain increasing ^{232}Th fluxes with depth unless the removal of ^{230}Th was decoupled from the removal of ^{232}Th. In the absence of a fractionating mechanism between the two isotopes, rapid, irreversible scavenging would similarly remove dissolved ^{232}Th, for example, the residence time of ^{230}Th would still be validly applied to ^{232}Th at each depth. The simultaneous rapid scavenging of ^{230}Th and ^{232}Th can be observed upon careful inspection of SO245 dissolved Th isotope profiles: At stations 4–10, $^{230}\text{Th}_d$ is constant, while $^{232}\text{Th}_d$ decreases slightly from the surface to the depth of the DCM (Figure 2). Interestingly, a similar

signature is seen in particulate ^{230}Th and ^{232}Th at these stations, albeit with much lower sampling resolution: constant $^{230}Th_p$ and decreasing $^{232}Th_p$ between the surface and DCM (Figure 3).

Like for dissolved ^{232}Th fluxes, there is also depth variability in particulate ^{230}Th-normalized ^{232}Th fluxes, complicating the choice of depth to use for evaluating dust fluxes. Fluxes computed by this method increase in the upper 1,000 m and are constant from 1,000 to 2,000 m (Figure 5a). A similar pattern has been observed in the North Atlantic, both in particulate ^{232}Th fluxes (Hayes, Black, et al., 2018) and in sediment traps (Huang & Conte, 2009) near the Bermuda Atlantic Time Series, attributed to lateral transport of lithogenic material from continental margins in the western Atlantic. Increasing $^{230}Th_p$-normalized ^{232}Th fluxes in size-fractionated < 51 μm particulate matter are also observed in the central North Atlantic, too far from coastal margins for lateral sediment transport to be important (Anderson et al., 2016). This was hypothesized to be due to rapid export of fine (<51 μm) lithogenic particles from the upper water column in large (>51 μm) aggregates, which subsequently disaggregate throughout the thermocline (Ohnemus & Lam, 2015).

On SO245, both dissolved and particulate ^{232}Th concentrations increase with depth between 300 and 1,000 m at stations 2–10 (Figure 3). One additional possibility to explain our increasing particulate ^{232}Th fluxes between these depths is that subsurface water masses at these depths carry a preformed dissolved ^{232}Th signature that re-equilibrates with the local particle field, driving increasing particulate ^{232}Th concentrations and fluxes. The primary water mass at these depths is Antarctic Intermediate Water (AAIW), with some Pacific Deepwater below 800–1,000 m (Fitzsimmons et al., 2016). The CFC-12 ventilation age of AAIW equatorward of 30°S in the South Pacific is at least 30 years (Hartin et al., 2011). The residence time of Th integrated across the upper 1,000 m at stations 2–10 is 8–12 years. Thus, a preformed signal originating in AAIW should be largely erased by the time it reaches our site. More data from AAIW formation regions, including on the upcoming meridional GEOTRACES GP17 section, will greatly improve our understanding of the effects of lateral transport on Th isotopes.

5.1.2. A New Mechanism for Depth-Dependent ^{232}Th Fluxes

The combined signature of increasing ^{232}Th flux in both the dissolved and particulate phases can be used to evaluate mechanisms that could cause these features. If we assume that the constant $^{232}Th_d$ fluxes with depth at 200–400 m and constant $^{232}Th_p$ fluxes below 1,000 m correctly represent the fluxes associated with dust deposition, we must explain why these estimates are too low near the surface. Simultaneous consideration of Equations 1 and 2 suggest that $^{232}Th_d$ fluxes are set by the balance between the production rate of ^{230}Th and the ratio of the inventories of the two Th isotopes $\frac{\int_0^z {}^{232}Th_d\, dz}{\int_0^z {}^{230}Th_d\, dz}$ (henceforth abbreviated I_{232}/I_{230}) integrated to depth z. Fluxes of $^{232}Th_p$ can be calculated using Equation 4, omitting the $[^{232}Th]_{dust}$ term, and reflect the balance between the production rate of ^{230}Th and the particulate ^{232}Th/^{230}Th ratio at depth z.

These observations suggest that the too-low $^{232}Th_d$ and $^{232}Th_p$ fluxes in the upper 200 m must be driven by process(es) that cause (1) lower than expected I_{232}/I_{230} and (2) lower than expected particulate ^{232}Th/^{230}Th ratios or (3) lower than expected ^{230}Th flux relative to production. In considering mechanisms for effecting depth-dependent ^{232}Th fluxes, it is useful to consider the one-dimensional mass balance for dissolved ^{230}Th:

$$\frac{dA}{dt} = 0 = P - J - u\frac{dA}{dx} + K_h\frac{d^2A}{dx^2} + K_z\frac{d^2A}{dz^2}. \quad (5)$$

P represents production by uranium decay, J is the net removal rate due to particle scavenging, u is a lateral advective velocity, K_h is the lateral diffusivity, K_z is the vertical diffusivity, and A is the activity of dissolved ^{230}Th. The mass budget of ^{232}Th is the same as in Equation 5, except there is no production rate by U decay: Instead, it is supplied to the surface by dust dissolution, where it is balanced by reversible scavenging removal. At steady state, these mass budgets result in linearly increasing dissolved ^{230}Th with depth and constant dissolved ^{232}Th with depth (Bacon & Anderson, 1982).

Since ^{230}Th increases with depth, it can experience net vertical redistribution by diapycnal diffusion. The lack of steady-state dissolved ^{232}Th gradients prevent this process from affecting its dissolved profiles. Thus, vertical mixing within and through the base of the mixed layer will cause there to be "too much" ^{230}Th in the mixed layer, driving high I_{230} and $[^{230}Th]_p$, and low I_{232}/I_{230} and particulate ^{232}Th/^{230}Th at

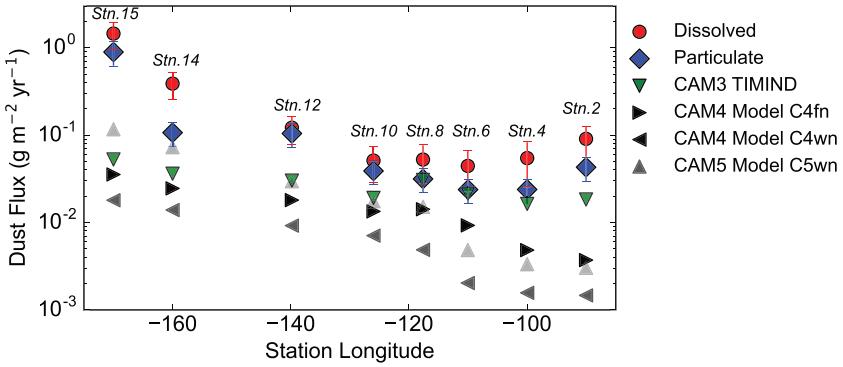

Figure 6. Observed and modeled dust fluxes at each station on the SO245 transect. Dissolved estimates of dust fluxes use 250 m integration depths and parameters described for calculating dust flux in Figure 4. Particulate estimates of dust flux were taken from 1,000 m depth as described in section 5.2. Modeled dust deposition rates from the nearest grid cell to sampling stations were extracted from CAM3 (Mahowald et al., 2006), and three separate model setups for CAM4 and CAM5 also described in section 5.2 (Albani et al., 2014).

shallow depths. As the inventory I_{230} is integrated deeper, to depths with greater concentrations of dissolved ^{230}Th, the bias induced by the mixed layer inventory is progressively reduced, resulting in dust fluxes that asymptotically approach the "true" value at some depth. We also note that this explanation can explain the apparent increase with depth in particulate dust fluxes (Figure 5).

Additional work, including both one-dimensional and global modeling efforts, will be needed to confirm our hypothesis regarding depth-dependent dust fluxes. In the absence of this, choosing an integration depth for both dissolved and particulate dust fluxes remains difficult. Given that dust fluxes derived from dissolved Th isotopes at stations 2–12 are constant with depth from 200 to 400 m, we choose 250 m as our integration depth for dust fluxes based on dissolved Th isotopes. While we lack depth resolution between the DCM and 1,000 m for particulate Th isotopes, since previous studies (Anderson et al., 2016) have found good agreement between coretop Th-based dust fluxes and particulate-based fluxes at 1,000 m, and since our particulate Th-based fluxes on SO245 are constant below 1,000 m, we use 1,000 m as representative to compute dust fluxes from particulate Th isotopes.

5.2. Dust Fluxes From Dissolved and Particulate ^{230}Th-^{232}Th in the South Pacific

Having established the depths to use for calculating dust fluxes from dissolved (250 m) and particulate (1,000 m) ^{230}Th-^{232}Th measurements, we now compare our estimates of dust flux between the two methods, with model estimates of dust deposition in the SPG, and with a compilation of ^{230}Th-normalized dust fluxes from surface sediments in the Pacific. Two additional variables must be defined for converting ^{232}Th fluxes for dust fluxes. In both the dissolved and particulate methods, the concentration of ^{232}Th in dust ($[^{232}\mathrm{Th}]_{\mathrm{dust}}$) is used to convert from calculated ^{232}Th fluxes to dust fluxes. The likely source regions for the entirety of the SO245 transect, western South America and Australia, have similar ^{232}Th concentrations of 14 ± 1 ppm in fine (<5 μm) fractions of sediments from likely dust source areas (McGee et al., 2016), and we adopt this value and its uncertainty for $[^{232}\mathrm{Th}]_{\mathrm{dust}}$. For dust fluxes from dissolved ^{230}Th-^{232}Th, the fractional solubility of thorium (S_{Th}) is an additional variable that must be assigned. S_{Th} remains poorly constrained, with a lower bound of 1% and an upper bound of 28% (Arraes-Mescoff et al., 2001; Hayes et al., 2017; Hayes, Anderson, Fleisher, et al., 2013; Hsieh et al., 2011; Roy-Barman et al., 2002). We adopt the most-recent estimate from of $S_{\mathrm{Th}} = 0.21 \pm 0.07$ Hayes et al. (2017) derived from comparing aerosol settling fluxes of ^{232}Th with 250-m integrated $^{232}\mathrm{Th}_d$ fluxes from the North Atlantic. We assume that thorium solubility remains constant with distance from dust source region, backed by a recent study finding that atmospheric processing of dust does not modify Th solubility in aerosols (Baker et al., 2020). For estimates of dust flux from particulate ^{230}Th-^{232}Th, we also introduce a nominal 30% uncertainty typically assigned to the assumption that ^{230}Th flux through a depth horizon is equal to its water column production rate (Henderson et al., 1999). Note however that this is not a random error, but one associated with the net lateral transport of ^{230}Th given the local/regional scavenging conditions at a given site.

Table 1
Dust Fluxes Derived From Dissolved Th-Based Estimates and Particulate Th-Based Estimates at SO245 Stations 2–12

Station	Latitude	Longitude	Dissolved Th-based dust flux (g/m^2/year)	Dissolved Th-based dust flux error (1σ)	Particulate Th-based dust flux (g/m^2/year)	Particulate Th-based dust flux error (1σ)
2	−23.5173	−90.0295	0.091	0.036	0.043	0.013
4	−23.501	−99.9916	0.055	0.029	0.024	0.007
6	−23.4904	−110.0391	0.044	0.022	0.024	0.007
8	−27.7421	−117.6207	0.053	0.025	0.032	0.010
10	−33.5	−125.9999	0.051	0.022	0.039	0.012
12	−39.3102	−139.8102	0.122	0.043	0.104	0.032

Note. Stations 14 and 15 are not included, as the apparent dust fluxes derived from Th isotopes are suspected to include lateral sources of lithogenic material in addition to that from dust deposition (see section 5.3). Dissolved Th-based estimates of dust fluxes use an integration depth of 250 m, and particulate Th-based dust fluxes use an integration depth of 1,000 m (sections 5.1 and 5.2).

Despite the numerous caveats associated with both methods employed here for determining dust flux, we find strong agreement between the two methods for most of the SO245 section. At seven of eight stations, dust fluxes from the two methods are within 1-sigma uncertainty (Figure 6). Dust fluxes from the two methods also follow a similar zonal pattern, decreasing westward from station 2 to station 6 and increasing westward from station 10 to station 15. Increasing fluxes at the furthest east and west ends of the section suggest that both Australia and South America serve as dust sources to the SPG.

Though the methods agree within stated uncertainties and show the same spatial pattern of dust flux in the South Pacific, there are consistent offsets observed between the two methods. Dust fluxes from the dissolved method are always higher than those from the particulate method. One possibility is that we have underestimated the solubility of Th—greater S_{Th} would decrease the dust flux estimates from dissolved Th isotopes. However, if the solubility of Th were the only reason for the discrepancy, the dissolved Th estimates of dust fluxes should be offset higher than particulate estimates by a constant factor, reflecting the factor by which S_{Th} has been overestimated. Instead, with the exception of station 14, we observe a zonal trend in the factor by which dissolved Th-based dust fluxes are higher. The dissolved Th dust estimates are 2.1–2.3 times greater at stations 2 and 4, decreasing monotonically to be 1.2 times greater at station 12, before increasing to be 1.6 times greater at station 15.

Regardless of the differences between our two methods, the consistency and reproducible spatial pattern of dust fluxes we have calculated provide valuable benchmarks for models of dust deposition to the open ocean. Few observations of dust flux are available to calibrate dust models over remote ocean regions like the SPG. The observations that exist typically rely on aerosol measurements and assumptions of settling velocities (dry deposition) and scavenging efficiency by precipitation (wet deposition). These aerosol-based estimates of dust flux also only provide a snapshot, integrated on weekly to monthly timescales. One such estimate from the SPG gave dust deposition rates 0.002–0.007 g/m^2/year, a full order of magnitude lower than our observations from thorium isotopes (Wagener et al., 2008). This discrepancy may be due to seasonality, which is important for dust emissions from Australia and South America (Mackie et al., 2008) with Th isotopes integrating across large dust deposition events missed during the timescales of aerosol sampling.

The dust input rates we calculate for the SPG (Table 1) are the lowest tracer-based estimates of dust flux observed to date in the world ocean. At SO245 stations 4 and 6, we find dust deposition rates of 0.02–0.05 g/m^2/year. These are an order of magnitude lower than dissolved Th-based estimates of dust flux in the Equatorial Pacific (Lopez et al., 2015) and subtropical North Pacific (Hayes et al., 2015), nearly two orders of magnitude lower than in the subpolar North Pacific (Hayes, Anderson, Fleisher, et al., 2013) and two to three orders of magnitude lower than in the subtropical North Atlantic (Anderson et al., 2016; Hsieh et al., 2011). Many more reconstructions of late-Holocene dust flux are available from surface sediment measurements of Th isotopes, compiled recently in the Thoromap database (Kienast et al., 2016). The lowest dust fluxes in the Thoromap database, from the Eastern Equatorial Pacific, are two to four times higher than those we measure at SO245 stations 4 and 6. A geographic pattern is emerging from dissolved thorium-based estimates of dust flux that is well-aligned with our understanding of dust source regions and prevailing wind patterns: highest inputs in the Atlantic, lower

inputs in the subtropical North Pacific and Equatorial Pacific, and lowest inputs in the remote subtropical South Pacific.

We compare our estimates with those from four realizations of dust models from the Community Earth System Model's Community Atmosphere Model (CAM): one from CAM3 using a slab ocean model and land model vegetation (CAM3 TIMIND; Mahowald et al., 2006) one from the CAM version 4 (CAM4) with model winds (C4fn), one from CAM4 with reanalysis winds (C4wn), and from CAM version 5 (CAM5) with reanalysis winds (C5wn). CAM4 and CAM5 model results are from Albani et al. (2014). The older CAM3 model is in much better agreement with our results from thorium isotopes in the eastern part of the SO245 section while CAM4 and CAM5 dust models underestimate thorium-derived dust fluxes by 1–2 orders of magnitude (Figure 6). The disagreement between models and observations is greatest in the eastern portion of the transect, suggestive of the models missing a South American dust source carried to the SPG by easterly trade winds. The broad model-data disagreement is consistent with previously noted model underestimation of Southern Hemisphere dust deposition compared to terrestrial archives (Albani et al., 2014). As atmospheric dust deposition models continue to be revised and updated, our estimates of dust flux (Table 1) should serve as an additional benchmark in the South Pacific. Given the extreme paucity of other measurements of Holocene dust fluxes in the South Pacific Ocean which could be used to validate model estimates (Kienast et al., 2016), we recommend caution when using modeled dust deposition to derive input rates of micronutrients like Fe to the South Pacific and other low-dust flux regions.

5.3. Iron Input Rates and Residence Times

The SPG is an important location for diagnosing dust-borne Fe fluxes. There have been significant mismatches between models (Deutsch et al., 2007) and observations (Knapp et al., 2016) of nitrogen fixation rates in the SE Pacific, hypothesized to be due in part to the inability of models to properly account for iron-limitation. Diazotrophs have much greater cellular Fe quotas than other phytoplankton types (Berman-Frank et al., 2001), due in part to the high Fe requirements of the nitrogenase enzymes used in nitrogen fixation (Raven, 1988; Whittaker et al., 2011). Quantifying iron fluxes from dust deposition across the SPG would be a critical step toward determining how much nitrogen fixation can take place in different regions and resolving model-data discrepancies in the spatial distribution of nitrogen fixation in the South Pacific.

Fluxes of soluble trace elements (here, Fe) can be determined from dissolved thorium isotopes via a modified form of Equation 3:

$$\text{Dissolved Fe Flux} = F\left(^{232}\text{Th}\right) * \left[\frac{\text{Fe}}{^{232}\text{Th}}\right]_{\text{dust}} * \frac{S_{\text{Fe}}}{S_{\text{Th}}}. \quad (6)$$

Rather than an absolute solubility, this requires knowledge of the fractional solubility ratio of Fe to Th, $S_{\text{Fe}}/S_{\text{Th}}$. There is significant variance across different leaching-based methods for determining the absolute solubility of Th and Fe in aerosols (Anderson et al., 2016). However, the relative solubility of Fe to Th is better established, with time-series observations of ^{232}Th and Fe in the surface ocean at Station Aloha suggesting $S_{\text{Fe}}/S_{\text{Th}}$ is close to 1 (Hayes et al., 2015), and acetic acid leaching of African dust samples produced $S_{\text{Fe}}/S_{\text{Th}}$ of 1.3 ± 0.3 (Hayes, Anderson, et al., 2018). Another plausible approach is to measure concentrations of acetic acid-soluble trace elements in aerosols from dust source areas supplying the study area. If concentrations of both soluble iron and thorium are measured in aerosols, the ratio of aerosol soluble Fe/Th (here denoted $[\text{Fe/Th}]_{\text{sol}}$) should reflect the product of $[\text{Fe/Th}]_{\text{dust}}$ multiplied by $S_{\text{Fe}}/S_{\text{Th}}$. Baker et al. (2016) performed these measurements off the coast of Peru between 6°S and 16°S, just to the north of the easternmost stations in our study area, finding $[\text{Fe/Th}]_{\text{sol}}$ of $6{,}220 \pm 1{,}990$ mol/mol. The 5-day air mass back trajectories from the sites of Baker et al. (2016) lead to nearby our station 2, suggesting that $[\text{Fe/Th}]_{\text{sol}} = 6{,}220 \pm 1{,}990$ is also indicative of the aerosols being deposited at our easternmost stations on SO245. However, this is 3.25 three times lower than the $[\text{Fe/Th}]_{\text{sol}} = 20{,}220 \pm 4{,}665$ derived by multiplying Fe/Th ratio in average upper continental crust (15,500 mol/mol) by $S_{\text{Fe}}/S_{\text{Th}} = 1.3 \pm 0.3$. Since we do not know the absolute value of $[\text{Fe/Th}]_{\text{sol}}$, we can only estimate iron input rates, and thus residence times, within this factor of 3.25. Finally, we note that we are assuming that $S_{\text{Fe}}/S_{\text{Th}}$ remains constant during atmospheric dust transport. While Th solubility is constant during aerosol transport (Baker et al., 2020), Fe solubility generally increases with decreasing

Table 2
Fe Fluxes and Residence Times at Each SO245 Station

Station	Lat.	Lon.	dFe dust flux (aerosol ratio) (μmol/m^2/year)	dFe dust flux (Baker ratio) (μmol/m^2/year)	dFe vertical flux (μmol/m^2/year)	dFe Inv. (μmol/m^2)	Fe res. time (year)
2	−23.517	−90.030	23.14 ± 7.10	7.15 ± 2.70	2.1	18.90 ± 0.83	0.75–2.0
4	−23.501	−99.992	13.93 ± 6.52	4.30 ± 2.23	2.3	18.60 ± 1.38	1.2–2.8
6	−23.490	−110.039	11.33 ± 4.82	3.50 ± 1.68			
8	−27.742	−117.621	13.40 ± 5.35	4.14 ± 1.89	0	27.08 ± 2.71	2.0–6.5
10	−33.500	−126.000	13.06 ± 4.62	4.03 ± 1.68			
12	−39.310	−139.810	31.05 ± 7.79	9.58 ± 3.21			
14	−39.000	−160.001	99.08 ± 23.27	30.59 ± 9.88			
15	−39.000	−170.001	370.25 ± 86.20	114.29 ± 36.73			

Note. Fe fluxes were calculated using Equation 6, integrated to 250 m. Residence times are similarly integrated to 250 m, calculated using Equation 7, with dFe inventories at SO245 stations 2 and 4 coming from stations 4 and 7 from Fitzsimmons et al. (2016), and the dFe inventory at SO245 station 8 coming from station GYR from Blain et al. (2008). The values given for dFe residence times reflect calculations using North American aerosol S_{Fe}/S_{Th} (lower residence time) versus the S_{Fe}/S_{Th} ratio from Baker et al. (2016) (higher residence time).

atmospheric dust loading (e.g., Sholkovitz et al., 2012). Thus, S_{Fe}/S_{Th} might be expected to increase with increasing distance from the dust source region. If this were the case, the dFe fluxes we compute using Equation 6 would be underestimated at our stations furthest from continental sources.

We find soluble Fe fluxes, integrated to 250 m, of 7–23 μmol/m^2/year at station 2, decreasing to 3.5–11 μmol/m^2/year at stations 4–10 in the center of the SPG, before increasing toward 114–370μmol/m^2/year at station 15 (Table 2). The dust-borne Fe fluxes to the SPG we derive using Equation 6 are comparable to one recent dust Fe flux estimate of 8.7 μmol/m^2/year from aerosol measurements (Buck et al., 2013). Another aerosol-based estimate of soluble iron to the SPG of 2.2–3.7 μmol/m^2/year (Wagener et al., 2008) is approximately three times lower than our fluxes using $[Fe/Th]_{sol}$ of North Atlantic aerosols but very similar to our fluxes determined using $[Fe/Th]_{sol}$ from Baker et al. (2016). Aerosol- and ^{7}Be-based estimates of Fe flux from the GEOTRACES GP16 transect further north than our study site have a similar range, of 0.5–3 μmol/m^2/year at their stations 17–30 (Buck et al., 2019). Fewer comparisons exist for the western portion of the transect. Based on rainwater Fe concentrations and an assumed annual precipitation rate at 32.5°S and 170°W, Ellwood et al. (2018) estimated dust Fe fluxes of 26.3 μmol/m^2/year, about five to 10 times lower than our estimate of 114–370 μmol/m^2/year at station 15. This discrepancy may indicate that a substantial portion of the dFe flux integrated to 250 m we compute at station 15 is derived from subsurface lateral transport of lithogenics dissolved on the Chatham Rise.

Where there are depth profiles of dissolved Fe coincident with Th-based estimates of dFe input rates, the residence time of iron can be determined by dividing the dissolved inventory at a given depth by the dissolved flux integrated to that depth determined from Equation 6:

$$\tau_{Fe} = \frac{I_{Fe}}{\text{dFe Flux}}. \quad (7)$$

While there were no measurements of dFe made on the SO245 cruise, there are published dFe profiles from within ~400 km of stations 2, 4, and 8. Dissolved Fe data collected at stations 4 and 7 from the BiG RAPA transect (Fitzsimmons et al., 2016) can be combined with Fe fluxes from SO245 stations 2 and 4, respectively, and dFe profiles from the BIOSOPE GYR station (Blain et al., 2008) can be combined with Fe fluxes from SO245 station 8 (Figure 1).

Calculating residence times of Fe from dFe fluxes derived from Th isotopes assumes that dust-borne Fe constitutes the primary Fe source at a given location. Fitzsimmons et al. (2016) argued that lateral diffusive fluxes of Fe from the South American shelf constituted the largest dFe source to the upper 250 m of the SPG by several orders of magnitude. However, their method (also used by Rijkenberg et al., 2012) for calculating lateral diffusive Fe fluxes makes several assumptions that warrant discussion. A conceptual error in these estimates and those of Labatut et al. (2014) is comparing vertical fluxes through a horizontal plane at a reference depth with lateral fluxes through a vertical plane parallel to the coast. A significant portion of this lateral flux could simply be transported further offshore. Rather than the lateral flux

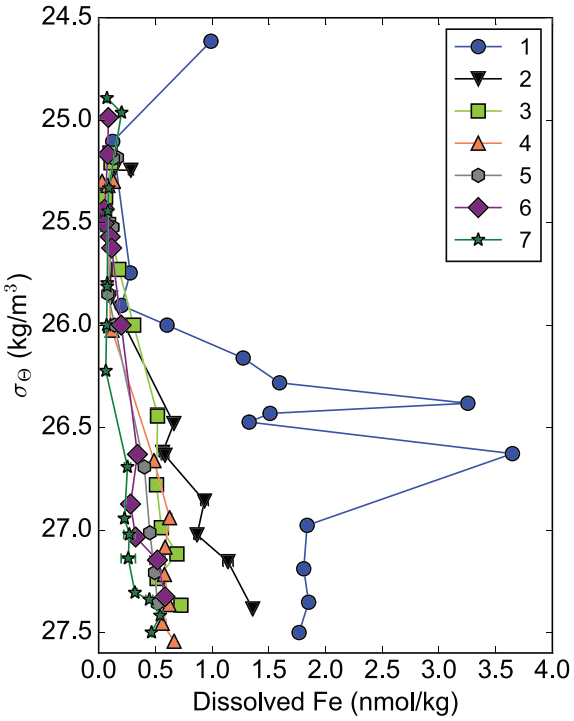

Figure 7. Profiles of dissolved Fe from Fitzsimmons et al. (2016) plotted against potential density (σ_Θ).

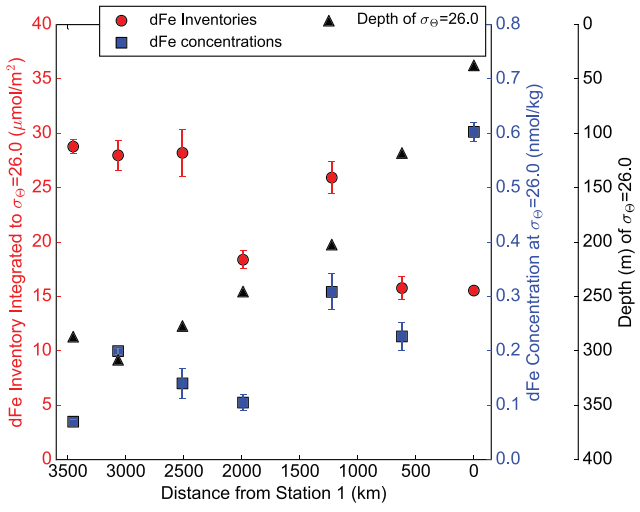

Figure 8. Characteristics of dissolved iron and physical setting from Southeast Pacific data of Fitzsimmons et al. (2016). Iron concentration at each station was linearly interpolated onto the $\sigma_\Theta = 26.0$ isopycnal, as was isopycnal depth. Red dots show dissolved Fe inventories integrated to the depth of $\sigma_\Theta = 26.0$ kg/m^3. Blue squares show the dissolved Fe concentration at $\sigma_\Theta = 26.0$ kg/m^3. Black triangles show depth of the $\sigma_\Theta = 26.0$ kg/m^3 isopycnal. Given the lack of gradient in dFe inventories integrated to $\sigma_\Theta = 26.0$, the minimal offshore dFe gradient at $\sigma_\Theta = 26.0$, and the depth of the $\sigma_\Theta = 26.0$ isopycnal plunging below 250 m moving offshore, isopycnal mixing will act to transport dFe offshore only at or below the upper 250 m, not to the surface of the South Pacific Gyre.

in, it is necessary to compute the convergence of lateral flux (i.e., the second derivative d^2[dFe]/dx^2, representing the balance of lateral fluxes in and out) to determine whether there is a net dFe supply at each station studied. Using only the input (output) flux terms to compute residence times, rather than the flux convergence, will result in a substantial overestimation of supply (removal) rates and underestimation of residence times.

We revisit the dFe gradients of Fitzsimmons et al. (2016) and show that far less Fe can be transported to the upper 250 m of the SPG by isopycnal mixing of coastal Fe than was inferred by Fitzsimmons et al. Near the South American continent, wind-driven upwelling brings deeper isopycnal layers close to the surface. The ferricline in the SPG observed by Fitzsimmons et al. (2016) was found below the potential density surface $\sigma_\Theta = 26.0$ kg/m^3 (Figure 7). The calculated dFe gradients both for deriving an apparent lateral diffusivity and for determining lateral fluxes in Fitzsimmons et al. (2016) were determined between the depth of the mixed layer and 250 m at each station. Because of the shoaling density layers near the South American continent, the dFe inventories at these stations encompass substantially different density layers: closer to the continent this integrates to potential densities up to $\sigma_\Theta = 26.6$ kg/m^3. Furthermore, the vast majority of the high dFe concentrations near the continent is found at these denser layers, with density greater than $\sigma_\Theta = 26.0$ kg/m^3 (Figure 7). There are negligible offshore dFe gradients at densities above $\sigma_\Theta = 26.0$ kg/m^3 (Figure 7), indicating that there cannot be substantial offshore transport of dFe by isopycnal mixing at lighter densities than this. At the offshore stations 4–7, since $\sigma_\Theta = 26.0$ kg/m^3 is found at ~250 m, this implies minimal transport of dFe by lateral diffusion into the upper 250 m. Dissolved Fe inventories integrated to the $\sigma_\Theta = 26.0$ kg/m^3 density horizon at each station from Fitzsimmons et al. (2016) actually increase moving offshore, due to the much shallower depth of the $\sigma_\Theta = 26.0$ kg/m^3 isopycnal nearshore (Figure 8). While there is a concentration gradient moving offshore at $\sigma_\Theta = 26.0$ kg/m^3, mixing will act to transport dFe along this isopycnal. By station 4, this isopycnal is at 250 m, the upper depth of the ferricline (Figure 8), indicating that lateral mixing will act to transport dFe at or below the upper 250 m, not within the upper 250 m. The correlation between dFe and AOU below 250 m (or $\sigma_\Theta = 26.0$ kg/m^3) in the SPG observed by Fitzsimmons et al. (2016) is likely due to the shared influence of diffusive mixing in transporting low-O_2 high-Fe waters from the continental shelf into the SPG at depth, rather than regeneration of Fe from above.

Since lateral mixing cannot supply substantial dFe to the upper 250 m of the SPG, the two remaining Fe fluxes important for computing τ_{Fe} are dust input and vertical mixing from below. Using diffusivity estimates from CTD profiles of vertical density gradients, Fitzsimmons et al. (2016) calculate vertical diffusive Fe supply rates of 2.1 and 2.3 μmol/m^2/year at 250 m for BiG RAPA stations 4 (SO245 station 2) and 7 (SO245 station 4), respectively. No vertical dFe gradient was observed by Blain et al. (2008) in the upper 400 m at the BIOSOPE GYR station (SO245 station 8), so a vertical supply term is not included in the τ_{Fe} calculation here. These vertical diffusive

dFe supply rates are a factor of 2–10 lower than the input rates we compute from dust input. In contrast to previous studies (a), we argue that atmospheric deposition, not physical transport, is the most important process supplying Fe to the surface of the SPG.

We compute τ_{Fe} using Equation 7, with I_{Fe} integrated to 250 m, using the sum of the vertical diffusive inputs as calculated in Fitzsimmons et al. (2016) and Th-based atmospheric dFe input rates (calculated using Equation 6, integrating to 250 m) for dFe flux. The Fe residence times increase moving offshore, from 0.75–2 years at station 2, to 1.2–2.8 years at station 4, to 2.0–6.5 years at station 8 (Table 2). These values are similar to the residence times of 0.5–1 years observed at 250 m at Station Aloha derived from the same method (Hayes et al., 2015), two to times times longer than 250 m estimates from the North Atlantic (Hayes, Anderson, et al., 2018), within the range of estimates from the GEOTRACES GP16 section equatorward of SO245 in the South Pacific (Kadko et al., 2020) but shorter than the residence time of dFe in the mixed layer inferred from the Southwest Pacific (Ellwood et al., 2018).

5.4. Biogeochemical Implications for Diazotrophy

Ideally, our estimates of iron input rates could be directly linked to its biogeochemical cycling by microorganisms at the sea surface. Connecting the large-scale geochemical budgets of trace elements with rates of specific metabolic functions in microbial communities has to date been difficult, as these parameters are generally not analyzed together on the same cruises, and their measurements often integrate over very different timescales. Here, we outline an approach to derive estimates on the upper limit of N_2-fixation rates that can be supported by a given rate of dust-borne Fe input. We note that many of the parameters in our approach may have significant uncertainties on them but discuss how future sampling efforts might allow for the connection between oceanic processes inferred from geochemical budgets and specific biological functions.

The first step in deriving upper limits on N_2-fixation rates from a given Fe flux is to define the input rate of bioavailable Fe. We use estimates of dust flux from Equation 3 multiplied by 3.5 wt% Fe in upper continental crust (Rudnick & Gao, 2014) to determine a bulk iron supply from dust (e.g., not just soluble Fe but all Fe). This term can be multiplied by a fractional bioavailability of Fe in dust, f_{bio}, to calculate the input of bioavailable iron from dust deposition $F_{Fe,bio}$:

$$F_{\text{Fe, bio}} = \text{Dust Flux} * [\text{Fe}]_{\text{UCC}} * f_{\text{bio}}. \quad (8)$$

The dust flux and crustal Fe terms are treated as knowns and have quantifiable uncertainties associated with them. The f_{bio} term is less well established. Typically, f_{bio} would be assumed to be equal to the solubility of Fe. However, this might vary depending on the local ecology. *Trichodesmium* and its epibiont are capable of solubilizing and accessing particulate Fe in dust particles (Basu et al., 2019; Rubin et al., 2011), so f_{bio} may be much greater than the 10% fractional solubility previously found for aerosol Fe in the Pacific (Buck et al., 2006). However, heterotrophs like unicellular Group A cyanobacteria (UCYN-A) (Halm et al., 2012) or *Gammaproteobacteria* (Moisander et al., 2014) may be responsible for the majority of N_2-fixation in the SPG, not *Trichodesmium*. There is no evidence to date that heterotrophic diazotrophs can solubilize iron from dust particles.

Using cellular stoichiometries for (Fe in nitrogenase):C and C:N, we can derive an upper bound on N_2-fixation (N_{fix}^{max}) that can be supported by a given Fe input rate:

$$N_{fix}^{max} = F_{\text{Fe, bio}} * \frac{\text{moles cellular C}}{\mu\text{mol Fe in Nitrogenase}} * \frac{\text{moles cellular N}}{\text{moles cellular C}}. \quad (9)$$

Our estimates of N_{fix}^{max} assume the following: (1) Every atom of new Fe supplied is bound in the nitrogenase enzyme of a diazotroph, (2) every atom of cellular N is fixed from N_2, and (3) Each enzymatic Fe atom is only used to fix nitrogen once. Since the dissolved Th-based estimates of dust flux from which Fe fluxes are derived integrate across 1–2 year timescales (i.e., the upper water column residence time of ^{230}Th), so too do our estimates of N_{fix}^{max}.

Table 3
Parameters Used to Calculate Upper Bounds on N_2-Fixation Using Average Dust Fluxes Derived From Th Isotopes at SO245 Stations 2–8, as Described in Section 5.4, Under Two Different Scenarios: One With Trichodesmium as the Dominant Diazotroph and One with Crocosphera as the Dominant Diazotroph

Organism	f_{bio}	$F_{Fe,bio}$ (μmol Fe/m^2/day)	Fe in nitrogenase:C (μmol/mol)	C:N (mol/mol)	N_{fix}^{max} (μmol N/m^2/day)
Trichodesmium	0.5	0.052	236:1	6.03	36.5
Crocosphera	0.1	0.010	15.8:1	8.6	76.5

Note. Cellular stoichiometries for *Trichodesmium* are from Whittaker et al. (2011) and Nuester et al. (2012). Cellular stoichiometries for *Crocosphera* are from Tuit et al. (2004).

As a proof of concept, we derive average N_{fix}^{max} values for SO245 stations 2–8 under two different scenarios (Table 3). In scenario 1, *Trichodesmium* is the dominant N_2-fixer, where $f_{bio} = 0.5$, (Fe in nitrogenase): C = 236:1 μmol/mol (Whittaker et al., 2011), and C:N = 6.03 ± 1.05 mol/mol (Nuester et al., 2012). In scenario 2, unicellular organisms are the dominant N_2-fixers. First, we assume $f_{bio} = 0.1$, the fractional Fe solubility in the region (Buck et al., 2006). Given the lack of data on cellular stoichiometries of uncultered UCYN-A and *Gammaproteobacteria*, we use values for the cyanobacteria *Crocosphera watsonii* of (Fe in nitrogenase):C = 15.8:1 μmol/mol and C:N = 8.6 mol/mol (Tuit et al., 2004).

The N_{fix}^{max} values we derive using average dust fluxes at SO245 stations 2–8 for the two scenarios described above are 36 μmol N/m^2/day for *Trichodesmium* and 76 μmol N/m^2/day for *Crocosphera* (Table 3). Comparing of our N_{fix}^{max} estimates with observations of N_2-fixation rates is complex, since measurements of N_2-fixation rates are typically performed using shipboard incubations lasting <24 hr (e.g., Montoya et al., 1996). Measurements of N_2-fixation rates at 20°S from 80°W to 100°W, just north of SO245 stations 2 and 4, occasionally exceeded our average N_{fix}^{max} values for both scenarios, reaching 98 μmol N/m^2/day at 100°W (Knapp et al., 2016). N_2-fixation rates of 191 μmol N/m^2/day previously measured at the same location as SO245 station 8 also exceeded both of our N_{fix}^{max} estimates (Halm et al., 2012). While there are large, difficult to quantify uncertainties associated with the cellular stoichiometries we have chosen, it is notable that measured N_2-fixation rates in the SPG are larger than both of our N_{fix}^{max} scenarios, since our N_{fix}^{max} calculations incorporate the likely-to-overestimate assumptions that every new Fe atom is used to fix N, and all cellular N is newly fixed.

We suggest three possible ways to explain how measured rates can exceed N_{fix}^{max}. First, either our choice of cellular stoichiometries could be incorrect, or there is a dominant N_2-fixing organism in the SPG (e.g., UCYN-A or *Gammaproteobacteria*) with significantly different cellular stoichiometries from *Trichodesmium* and *Crocosphera*. Second, short-term N_2-fixation rates may respond to episodic dust supply events depositing Fe to the surface ocean at rates above the long-term average (Guieu et al., 2014). Third, organisms may be using the same Fe atoms in nitrogenase enzymes to fix N_2 multiple times, violating our assumption of single use. The geochemical phenomenon of Fe recycling has been modeled to be important in regulating primary productivity in the Equatorial Pacific (Rafter et al., 2017). We suggest that Fe recycling could also be critical in relieving diazotrophs of Fe stress in the SPG. Indeed, *C. watsonii* has the ability to share cellular Fe between enzymes for N_2-fixation and photosynthesis (Saito et al., 2011), constituting a biochemical mechanism for regulating the Fe recycling inferred from geochemical fluxes. While we cannot yet resolve between the three possibilities, targeted work combining steady-state geochemical budgets of micronutrients with proteomic, transcriptomic, and other microbiological approaches will provide an avenue forward for delineating between the three mechanisms for Fe-diazotrophy connections we have described above.

6. Conclusions and Outlook for Future Work

We have provided new constraints on dust deposition, iron cycling, and biogeochemical dynamics in the South Pacific from measurements of water column thorium isotopes. However there are still ample opportunities remaining for future research to improve our understanding of these processes and their connections.

We argue that vertical diffusive redistribution of ^{230}Th into and within the surface mixed layer is responsible for the depth dependency of dissolved ^{232}Th fluxes in the upper water column. An increased number of global climate models are now simulating ^{230}Th distributions (Gu & Liu, 2017; Heinze et al., 2018; Rempfer et al., 2017; van Hulten et al., 2018). Incorporating ^{232}Th into these models, which have known dust flux fields, could facilitate testing our vertical mixing hypothesis and other mechanisms for generating depth-dependent ^{232}Th fluxes.

Our results show that models of dust flux may systematically underestimate deposition in the central and eastern SPG by 1–2 orders of magnitude. Studies relying on modeled dust deposition to derive estimates of elemental input rates in these regions should consider them to be a lower bound. The residence times of 0.75–6.5 years we derived for dissolved iron are consistent with previous observations from oligotrophic settings. Future work could constrain the input rates and residence times of additional trace elements besides iron in the South Pacific. Studies of ocean trace elements are expanding to more closely connect with biological activity via transcriptomic, metabolic, and proteomic studies through emerging programs like BIOGEOSCAPES (https://www.biogeoscapes.org/). Thorium-based estimates of soluble micronutrient fluxes would be a valuable contribution to work of this nature, as the distributions of gene expression, metabolite production, and elemental turnover rates by microorganisms can, in theory, be directly linked to geographic patterns in elemental supply.

Data Availability Statement

Dissolved and particulate ^{230}Th and ^{232}Th data from this study are archived at the Biological and Chemical Oceanography Data Management Office (https://www.bco-dmo.org/project/810771) and on Pangaea (dissolved: https://doi.pangaea.de/10.1594/PANGAEA.913219, particulate: https://doi.pangaea.de/10.1594/PANGAEA.913220).

Acknowledgments
This work was supported by U.S. National Science Foundation Grant OCE-1555726 to LDEO and an NSF Graduate Research Fellowship to F.J.P. (DGE-1644869). The UltraPac Expedition (SO245) was funded by the Federal Ministry of Education and Research of Germany (Grant 03G0245A). We thank the captain and crew of the *FS Sonne*, as well as SO245 Chief Scientist Tim Ferdelman for ensuring safe and successful sampling. We are grateful to Bernhard Fuchs, Claudia Ehlert, and Sebastian Vivancos for assistance with water sampling, pump deployment, and recovery on SO245. Comments from two anonymous reviewers and the associate editor greatly improved the paper.

References

Albani, S., Mahowald, N. M., Perry, A. T., Scanza, R. A., Zender, C. S., Heavens, N. G., et al. (2014). Improved dust representation in the Community Atmosphere Model. *Journal of Advances in Modeling Earth Systems*, *6*, 541–570. https://doi.org/10.1002/2013MS000279

Anderson, R. F., Cheng, H., Edwards, R. L., Fleisher, M. Q., Hayes, C. T., Huang, K. F., et al. (2016). How well can we quantify dust deposition to the ocean? *Philosophical Transactions A Mathematical, Physical and Engineering Sciences*, *374*(2081), 20150285. https://doi.org/10.1098/rsta.2015.0285

Anderson, R. F., Fleisher, M. Q., Robinson, L. F., Edwards, R. L., Hoff, J. A., Moran, S. B., et al. (2012). GEOTRACES intercalibration of ^{230}Th, ^{232}Th, ^{231}Pa, and prospects for ^{10}Be. *Progress in Oceanography*, *10*(4), 179–213. https://doi.org/10.4319/lom.2012.10.179

Arraes-Mescoff, R., Roy-Barman, M., Coppola, L., Souhaut, M., Tachikawa, K., Jeandel, C., et al. (2001). The behavior of Al, Mn, Ba, Sr, REE and Th isotopes during in vitro degradation of large marine particles. *Marine Chemistry*, *73*(1), 1–19. https://doi.org/10.1016/S0304-4203(00)00065-7

Bacon, M. P., & Anderson, R. F. (1982). Distribution of thorium isotopes between dissolved and particulate forms in the Deep Sea. *Journal of Geophysical Research*, *59*(6), 1817–1835. https://doi.org/10.1111/j.1365-3091.2012.01327.x

Baker, A. R., Li, M., & Chance, R. (2020). Trace metal fractional solubility in size-segregated aerosols from the tropical eastern Atlantic Ocean. *Global Biogeochemical Cycles*, *34*(6), e2019GB006510. https://doi.org/10.1029/2019GB006510

Baker, A. R., Thomas, M., Bange, H. W., & Plasencia Sánchez, E. (2016). Soluble trace metals in aerosols over the tropical south-east Pacific offshore of Peru. *Biogeosciences*, *13*(3), 817–825. https://doi.org/10.5194/bg-13-817-2016

Basu, S., Gledhill, M., de Beer, D., Prabhu Matondkar, S. G., & Shaked, Y. (2019). Colonies of marine cyanobacteria *Trichodesmium* interact with associated bacteria to acquire iron from dust. *Communications Biology*, *2*(1), 284. https://doi.org/10.1038/s42003-019-0534-z

Berman-Frank, I., Cullen, J. T., Shaked, Y., Sherrell, R. M., & Falkowski, P. G. (2001). Iron availability, cellular iron quotas, and nitrogen fixation in *Trichodesmium*. *Limnology and Oceanography*, *46*(6), 1249–1260. https://doi.org/10.4319/lo.2001.46.6.1249

Blain, S., Bonnet, S., & Guieu, C. (2008). Dissolved iron distribution in the tropical and sub tropical South Eastern Pacific. *Biogeosciences*, *5*(1), 269–280. https://doi.org/10.5194/bg-5-269-2008

Bonnet, S., Guieu, C., Bruyant, F., Prášil, O., van Wambeke, F., Raimbault, P., et al. (2008). Nutrient limitation of primary productivity in the Southeast Pacific (BIOSOPE cruise). *Biogeosciences*, *5*(1), 215–225. https://doi.org/10.5194/bg-5-215-2008

Buck, C. S., Aguilar-Islas, A., Marsay, C., Kadko, D., & Landing, W. M. (2019). Trace element concentrations, elemental ratios, and enrichment factors observed in aerosol samples collected during the US GEOTRACES eastern Pacific Ocean transect (GP16). *Chemical Geology*, *511*, 212–224. https://doi.org/10.1016/j.chemgeo.2019.01.002

Buck, C. S., Landing, W. M., & Resing, J. (2013). Pacific Ocean aerosols: Deposition and solubility of iron, aluminum, and other trace elements. *Marine Chemistry*, *157*, 117–130. https://doi.org/10.1016/j.marchem.2013.09.005

Buck, C. S., Landing, W. M., Resing, J. A., & Lebon, G. T. (2006). Aerosol iron and aluminum solubility in the northwest Pacific Ocean: Results from the 2002 IOC cruise. *Geochemistry Geophysics Geosystems*, *7*, Q04M07. https://doi.org/10.1029/2005GC000977

Claustre, H., Sciandra, A., & Vaulot, D. (2008). Introduction to the special section bio-optical and biogeochemical conditions in the South East Pacific in late 2004: The BIOSOPE program. *Biogeosciences*, *5*(3), 679–691. https://doi.org/10.5194/bg-5-679-2008

Costa, K. M., Hayes, C. T., Anderson, R. F., Pavia, F. J., Bausch, A., Deng, F., et al. (2020). ^{230}Th normalization: New insights on an essential tool for quantifying sedimentary fluxes in the modern and Quaternary ocean. *Paleoceanography and Paleoclimatology*, *35*(2), 387. https://doi.org/10.1029/2019PA003820

Deng, F., Thomas, A. L., Rijkenberg, M. J. A., & Henderson, G. M. (2014). Controls on seawater ^{231}Pa, ^{230}Th and ^{232}Th concentrations along the flow paths of deep waters in the Southwest Atlantic. *Earth and Planetary Science Letters*, *390*, 93–102. https://doi.org/10.1016/j.epsl.2013.12.038

Deutsch, C., Sarmiento, J. L., Sigman, D. M., Gruber, N., & Dunne, J. P. (2007). Spatial coupling of nitrogen inputs and losses in the ocean. *Nature*, *445*(7124), 163–167. https://doi.org/10.1038/nature05392

Ellwood, M. J., Bowie, A. R., Baker, A., Gault-Ringold, M., Hassler, C., Law, C. S., et al. (2018). Insights into the biogeochemical cycling of Iron, nitrate, and phosphate across a 5,300 km South Pacific zonal section (153°E–150°W). *Global Biogeochemical Cycles*, *32*, 187–207. https://doi.org/10.1002/2017GB005736

Fitzsimmons, J. N., Conway, T. M., Lee, J. M., Kayser, R., Thyng, K. M., John, S. G., & Boyle, E. A. (2016). Dissolved iron and iron isotopes in the southeastern Pacific Ocean. *Global Biogeochemical Cycles*, *30*, 1372–1395. https://doi.org/10.1002/2015GB005357

Gu, S., & Liu, Z. (2017). ^{231}Pa and ^{230}Th in the ocean model of the Community Earth System Model (CESM1.3). *Geoscientific Model Development*, *10*(12), 4723–4742. https://doi.org/10.5194/gmd-10-4723-2017

Guieu, C., Aumont, O., Paytan, A., Bopp, L., Law, C. S., Mahowald, N., et al. (2014). The significance of the episodic nature of atmospheric deposition to low nutrient low chlorophyll regions. *Global Biogeochemical Cycles*, *28*, 1179–1198. https://doi.org/10.1002/2014GB004852

Halm, H., Lam, P., Ferdelman, T. G., Lavik, G., Dittmar, T., LaRoche, J., et al. (2012). Heterotrophic organisms dominate nitrogen fixation in the South Pacific Gyre. *The ISME Journal*, *6*(6), 1238–1249. https://doi.org/10.1038/ismej.2011.182

Hartin, C. A., Fine, R. A., Sloyan, B. M., Talley, L. D., Chereskin, T. K., & Happell, J. (2011). Formation rates of Subantarctic Mode Water and Antarctic Intermediate Water within the South Pacific. *Deep Sea Research Part I: Oceanographic Research Papers*, *58*(5), 524–534. https://doi.org/10.1016/j.dsr.2011.02.010

Hayes, C. T., Anderson, R. F., Cheng, H., Conway, T. M., Edwards, R. L., Fleisher, M. Q., et al. (2018). Replacement times of a spectrum of elements in the North Atlantic based on thorium supply. *Global Biogeochemical Cycles*, *32*, 1294–1311. https://doi.org/10.1029/2017GB005839

Hayes, C. T., Anderson, R. F., Fleisher, M. Q., Serno, S., Winckler, G., & Gersonde, R. (2013). Quantifying lithogenic inputs to the North Pacific Ocean using the long-lived thorium isotopes. *Earth and Planetary Science Letters*, *383*, 16–25. https://doi.org/10.1016/j.epsl.2013.09.025

Hayes, C. T., Anderson, R. F., Jaccard, S. L., Francois, R., Fleisher, M. Q., Soon, M., & Gersonde, R. (2013). A new perspective on boundary scavenging in the North Pacific Ocean. *Earth and Planetary Science Letters*, *369-370*, 86–97. https://doi.org/10.1016/j.epsl.2013.03.008

Hayes, C. T., Black, E. E., Anderson, R. F., Baskaran, M., Buesseler, K. O., Charette, M. A., et al. (2018). Flux of particulate elements in the North Atlantic Ocean constrained by multiple radionuclides. *Global Biogeochemical Cycles*, *32*, 1738–1758. https://doi.org/10.1029/2018GB005994

Hayes, C. T., Fitzsimmons, J. N., Boyle, E. A., McGee, D., Anderson, R. F., Weisend, R., & Morton, P. L. (2015). Thorium isotopes tracing the iron cycle at the Hawaii Ocean Time-series Station ALOHA. *Geochimica et Cosmochimica Acta*, *169*, 1–16. https://doi.org/10.1016/j.gca.2015.07.019

Hayes, C. T., Rosen, J., McGee, D., & Boyle, E. A. (2017). Thorium distributions in high- and low-dust regions and the significance for iron supply. *Global Biogeochemical Cycles*, *31*, 328–347. https://doi.org/10.1002/2016GB005511

Heinze, C., Ilyina, T., & Gehlen, M. (2018). The potential of ^{230}Th for detection of ocean acidification impacts on pelagic carbonate production. *Biogeosciences*, *15*(11), 3521–3539. https://doi.org/10.5194/bg-15-3521-2018

Henderson, G. M., Heinze, C., Anderson, R. F., & Winguth, A. M. E. (1999). Global distribution of the flux to ocean sediments constrained by GCM modelling. *Deep Sea Research Part I: Oceanographic Research Papers*, *46*(11), 1861–1893. https://doi.org/10.1016/S0967-0637(99)00030-8

Hirose, K., & Sugimura, Y. (1987). Thorium isotopes in the surface air of the Western North Pacific Ocean. *Journal of Environmental Radioactivity*, *5*(6), 459–475. https://doi.org/10.1016/0265-931X(87)90020-8

Hsieh, Y.-T., Henderson, G. M., & Thomas, A. L. (2011). Combining seawater ^{232}Th and ^{230}Th concentrations to determine dust fluxes to the surface ocean. *Earth and Planetary Science Letters*, *312*(3–4), 280–290. https://doi.org/10.1016/j.epsl.2011.10.022

Huang, S., & Conte, M. H. (2009). Source/process apportionment of major and trace elements in sinking particles in the Sargasso sea. *Geochimica et Cosmochimica Acta*, *73*(1), 65–90. https://doi.org/10.1016/j.gca.2008.08.023

Jickells, T. D., An, Z. S., Andersen, K. K., Baker, A. R., Bergametti, G., Brooks, N., et al. (2005). Global iron connections between desert dust, ocean biogeochemistry, and climate. *Science*, *308*(5718), 67–71. https://doi.org/10.1126/science.1105959

Kadko, D., Aguilar-Islas, A., Buck, C. S., Fitzsimmons, J. N., Landing, W. M., Shiller, A., et al. (2020). Sources, fluxes and residence times of trace elements measured during the U.S. GEOTRACES East Pacific Zonal Transect. *Marine Chemistry*, *222*, 103781. https://doi.org/10.1016/j.marchem.2020.103781

Kienast, S. S., Winckler, G., Lippold, J., Albani, S., & Mahowald, N. M. (2016). Tracing dust input to the global ocean using thorium isotopes in marine sediments: ThoroMap. *Global Biogeochemical Cycles*, *30*, 1526–1541. https://doi.org/10.1002/2016GB005408

Knapp, A. N., Casciotti, K. L., Berelson, W. M., Prokopenko, M. G., & Capone, D. G. (2016). Low rates of nitrogen fixation in eastern tropical South Pacific surface waters. *PNAS*, *113*(16), 4398–4403. https://doi.org/10.1073/pnas.1515641113

Labatut, M., Lacan, F., Pradoux, C., Chmeleff, J., Radic, A., Murray, J. W., et al. (2014). Iron sources and dissolved-particulate interactions in the seawater of the Western Equatorial Pacific, iron isotope perspectives. *Global Biogeochemical Cycles*, *28*(10), 1044–1065. https://doi.org/10.1002/2014GB004928

Lamy, F., Gersonde, R., Winckler, G., Esper, O., Jaeschke, A., Kuhn, G., et al. (2014). Increased dust deposition in the Pacific Southern Ocean during glacial periods. *Science*, *343*(6169), 403–407. https://doi.org/10.1126/science.1245424

Lopez, G. I., Marcantonio, F., Lyle, M., & Lynch-Stieglitz, J. (2015). Dissolved and particulate ^{230}Th–^{232}Th in the Central Equatorial Pacific Ocean: Evidence for far-field transport of the East Pacific Rise hydrothermal plume. *Earth and Planetary Science Letters*, *431*, 87–95. https://doi.org/10.1016/j.epsl.2015.09.019

Mackie, D. S., Boyd, P. W., McTainsh, G. H., Tindale, N. W., Westberry, T. K., & Hunter, K. A. (2008). Biogeochemistry of iron in Australian dust: From eolian uplift to marine uptake. *Geochemistry, Geophysics, Geosystems*, *9*, Q03Q08. https://doi.org/10.1029/2007GC001813

Mahowald, N. M., Baker, A. R., Bergametti, G., Brooks, N., Duce, R. A., Jickells, T. D., et al. (2005). Atmospheric global dust cycle and iron inputs to the ocean. *Global Biogeochemical Cycles*, *19*, GB4025. https://doi.org/10.1029/2004GB002402

Mahowald, N. M., Muhs, D. R., Levis, S., Rasch, P. J., Yoshioka, M., Zender, C. S., & Luo, C. (2006). Change in atmospheric mineral aerosols in response to climate: Last glacial period, preindustrial, modern, and doubled carbon dioxide climates. *Journal of Geophysical Research*, *111*, D10202. https://doi.org/10.1029/2005JD006653

Martínez-Garcia, A., Sigman, D. M., Ren, H., Anderson, R. F., Straub, M., Hodell, D. A., et al. (2014). Iron fertilization of the Subantarctic Ocean during the Last Ice Age. *Science*, *343*(6177), 1347–1350. https://doi.org/10.1126/science.1246848

McGee, D., Winckler, G., Borunda, A., Serno, S., Anderson, R. F., Recasens, C., et al. (2016). Tracking eolian dust with helium and thorium: Impacts of grain size and provenance. *Geochimica et Cosmochimica Acta*, *175*, 47–67. https://doi.org/10.1016/j.gca.2015.11.023

Measures, C. I., & Brown, E. T. (1996). Estimating dust input to the Atlantic Ocean using surface water aluminium concentrations. In *The impact of desert dust across the Mediterranean* (Vol. 11, pp. 301–311). Dordrecht: Springer Netherlands. https://doi.org/10.1007/978-94-017-3354-0_30

Measures, C. I., & Vink, S. (2000). On the use of dissolved aluminum in surface waters to estimate dust deposition to the ocean. *Global Biogeochemical Cycles*, *14*, 317–327. https://doi.org/10.1029/1999GB001188

Moisander, P. H., Serros, T., Paerl, R. W., Beinart, R. A., & Zehr, J. P. (2014). Gammaproteobacterial diazotrophs and nifH gene expression in surface waters of the South Pacific Ocean. *The ISME Journal*, *8*(10), 1962–1973. https://doi.org/10.1038/ismej.2014.49

Montoya, J. P., Voss, M., Kahler, P., & Capone, D. G. (1996). A simple, high-precision, high-sensitivity tracer assay for N_2 fixation. *Applied and Environmental Microbiology*, *62*(3), 986–993. https://doi.org/10.1128/AEM.62.3.986-993.1996

Moore, C. M., Mills, M. M., Arrigo, K. R., Berman-Frank, I., Bopp, L., Boyd, P. W., et al. (2013). Processes and patterns of oceanic nutrient limitation. *Nature Geoscience*, *6*(9), 701–710. https://doi.org/10.1038/ngeo1765

Moore, C. M., Mills, M. M., Achterberg, E. P., Geider, R. J., LaRoche, J., Lucas, M. I., et al. (2009). Large-scale distribution of Atlantic nitrogen fixation controlled by iron availability. *Nature Geoscience*, *2*(12), 867–871. https://doi.org/10.1038/ngeo667

Moore, W. S., & Sackett, W. M. (1964). Uranium and thorium series inequilibrium in sea water. *Journal of Geophysical Research*, *69*(24), 5401–5405. https://doi.org/10.1029/JZ069i024p05401

Nuester, J., Vogt, S., Newville, M., Kustka, A. B., & Twining, B. S. (2012). The unique biogeochemical signature of the marine diazotroph *Trichodesmium*. *Frontiers in Microbiology*, *3*. https://doi.org/10.3389/fmicb.2012.00150

Ohnemus, D. C., & Lam, P. J. (2015). Cycling of lithogenic marine particles in the US GEOTRACES North Atlantic transect. *Deep Sea Research Part II: Topical Studies in Oceanography*, *116*, 283–302. https://doi.org/10.1016/j.dsr2.2014.11.019

Pavia, F., Anderson, R., Vivancos, S., Fleisher, M., Lam, P., Lu, Y., et al. (2018). Intense hydrothermal scavenging of ^{230}Th and ^{231}Pa in the deep Southeast Pacific. *Marine Chemistry*, *201*, 212–228. https://doi.org/10.1016/j.marchem.2017.08.003

Pavia, F. J., Anderson, R. F., Lam, P. J., Cael, B. B., Vivancos, S. M., Fleisher, M. Q., et al. (2019). Shallow particulate organic carbon regeneration in the South Pacific Ocean. *PNAS*, *116*(20), 9753–9758. https://doi.org/10.1073/pnas.1901863116

Rafter, P. A., Sigman, D. M., & Mackey, K. R. M. (2017). Recycled iron fuels new production in the eastern equatorial Pacific Ocean. *Nat Comms*, *8*(1), 1100. https://doi.org/10.1038/s41467-017-01219-7

Raven, J. A. (1988). The iron and molybdenum use efficiencies of plant growth with different energy, carbon and nitrogen sources. *The New Phytologist*, *109*(3), 279–287. https://doi.org/10.1111/j.1469-8137.1988.tb04196.x

Rempfer, J., Stocker, T. F., Joos, F., Lippold, J., & Jaccard, S. L. (2017). New insights into cycling of ^{231}Pa and ^{230}Th in the Atlantic Ocean. *Earth and Planetary Science Letters*, *468*, 27–37. https://doi.org/10.1016/j.epsl.2017.03.027

Rijkenberg, M. J. A., Steigenberger, S., Powell, C. F., van Haren, H., Patey, M. D., Baker, A. R., & Achterberg, E. P. (2012). Fluxes and distribution of dissolved iron in the eastern (sub-) tropical North Atlantic Ocean. *Global Biogeochemical Cycles*, *26*, GB3004. https://doi.org/10.1029/2011GB004264

Roy-Barman, M., Coppola, L., & Souhaut, M. (2002). Thorium isotopes in the western Mediterranean Sea: An insight into the marine particle dynamics. *Earth and Planetary Science Letters*, *196*(3–4), 161–174. https://doi.org/10.1016/S0012-821X(01)00606-9

Rubin, M., Berman-Frank, I., & Shaked, Y. (2011). Dust- and mineral-iron utilization by the marine dinitrogen-fixer *Trichodesmium*. *Nature Geoscience*, *4*(8), 529–534. https://doi.org/10.1038/ngeo1181

Rudnick, R. L., & Gao, S. (2014). Composition of the continental crust. In *Treatise on geochemistry* (pp. 1–51). Oxford, UK: Elsevier.

Saito, M. A., Bertrand, E. M., Dutkiewicz, S., Bulygin, V. V., Moran, D. M., Monteiro, F. M., et al. (2011). Iron conservation by reduction of metalloenzyme inventories in the marine diazotroph *Crocosphaera watsonii*. *PNAS*, *108*(6), 2184–2189. https://doi.org/10.1073/pnas.1006943108

Sholkovitz, E. R., Sedwick, P. N., Church, T. M., Baker, A. R., & Powell, C. F. (2012). Fractional solubility of aerosol iron: Synthesis of a global-scale data set. *Geochimica et Cosmochimica Acta*, *89*, 173–189. https://doi.org/10.1016/j.gca.2012.04.022

Tagliabue, A., Aumont, O., DeAth, R., Dunne, J. P., Dutkiewicz, S., Galbraith, E., et al. (2016). How well do global ocean biogeochemistry models simulate dissolved iron distributions? *Global Biogeochemical Cycles*, *30*, 149–174. https://doi.org/10.1002/2015GB005289

Tuit, C., Waterbury, J., & Ravizza, G. (2004). Diel variation of molybdenum and iron in marine diazotrophic cyanobacteria. *Limnology and Oceanography*, *49*(4), 978–990. https://doi.org/10.4319/lo.2004.49.4.0978

van Hulten, M., Dutay, J.-C., & Roy-Barman, M. (2018). A global scavenging and circulation ocean model of thorium-230 and protactinium-231 with improved particle dynamics (NEMO–ProThorP 0.1). *Geoscientific Model Development*, *11*(9), 3537–3556. https://doi.org/10.5194/gmd-11-3537-2018

Wagener, T., Guieu, C., Losno, R., Bonnet, S., & Mahowald, N. (2008). Revisiting atmospheric dust export to the Southern Hemisphere ocean: Biogeochemical implications. *Global Biogeochemical Cycles*, *22*, GB2006. https://doi.org/10.1029/2007GB002984

Whittaker, S., Bidle, K. D., Kustka, A. B., & Falkowski, P. G. (2011). Quantification of nitrogenase in *Trichodesmium* IMS 101: Implications for iron limitation of nitrogen fixation in the ocean. *Environmental Microbiology Reports*, *3*(1), 54–58. https://doi.org/10.1111/j.1758-2229.2010.00187.x